

Article

Mini Inside-Out Nuclear Magnetic Resonance Sensor Design for Soil Moisture Measurements

Jiamin Wu ¹ , Pan Guo ^{2,*}, Sheng Shen ¹, Yucheng He ¹, Xin Huang ¹ and Zheng Xu ^{1,*}

¹ State Key Laboratory of Power Transmission Equipment and System Security and New Technology, Chongqing University, Chongqing 400044, China; wujiamin@cqu.edu.cn (J.W.); shensheng@cqu.edu.cn (S.S.); heyucheng@cqu.edu.cn (Y.H.); xinhuang@cqu.edu.cn (X.H.)

² School of Physics and Electronic Engineering, Chongqing Normal University, Chongqing 401331, China

* Correspondence: guopan@cqu.edu.cn (P.G.); xuzheng@cqu.edu.cn (Z.X.);
Tel.: +86-135-2747-2600 (P.G.); +86-135-2747-5882 (Z.X.)

Received: 6 March 2019; Accepted: 3 April 2019; Published: 9 April 2019



Abstract: The improvement of water management in agriculture by exactly detecting moisture parameters of soil is crucial. To investigate this problem, a mini inside-out nuclear magnetic resonance sensor (NMR) was proposed to measure moisture parameters of model soils. This sensor combines three cylindrical magnets that are magnetized in the axial direction and three arc spiral coils of the same size in series. We calculated and optimized the magnet structure by equivalent magnetization to current density. By adjusting the radius and height between the cylinders, a circumferential symmetric constant gradient field (2.28 T/m) was obtained. The NMR sensor was set at 2.424 MHz to measure the water content of sandy soil with small particle diameter and silica sand with large particle diameter. The complete decaying, an NMR signal was analyzed through inverse Laplace transformation and averaged on a T_2 space. According to the results, moisture content of the sample is positively correlated with the integral area of T_2 spectrum peak (A_{peak}); T_2 of the water in small pores is shorter than that in large pores, because the movement of water molecules are limited by the inner wall of the pores. In the same volume, water in large pore sample is more than that in small pore sample, so A_{peak} of silica sand is larger than A_{peak} of sandy soil. Therefore, the sensor is capable of detecting moisture both content and pore size of the sample. This mini sensor (4.0 cm in diameter and 10 cm in length) is portable, and the lowest measurable humidity is 0.38%. Thus, this sensor will allow easy soil moisture measurements on-field in the future.

Keywords: agriculture; inside-out nuclear magnetic resonance; constant gradient field; soil moisture

1. Introduction

The improvement of water management in agricultural and geological explorations by detecting moisture parameters of soil exactly is crucial. However, investigating such parameters is time-consuming and invasive in many cases. Thus, a fast and noninvasive approach is required to examine the moisture parameters of soils [1]. In the last few decades, nuclear magnetic resonance (NMR) has broadened its range of applications due to some new methods that use inhomogeneous static magnetic fields. The introduction of mobile NMR devices has been an important evidence that supports these new ideas. Inside-out NMR has found important new applications in the oil industry [2,3], hydrological studies [1,4], and medicine [5].

In the inside-out style of measurement, the measured object is outside of the magnet; that is, the magnetic field is open and, therefore, inhomogeneous. The natural measurement geometry is that of a borehole where the sensor may be displaced longitudinally through the sample. Given that boreholes have a circular cross section, the ideal sensitive volume for the inside-out NMR is toroidal in shape.

Numerous magnet designs and applications have been suggested for the inside-out NMR. Jackson [6,7] proposed two cylindrical magnets of the same size, with opposing poles (SN–NS), to produce a toroidal region of a static field external to the apparatus. A simple solenoid coil located between the magnets produced a radiofrequency (RF) field B_1 , orthogonal to B_0 in the toroidal region. Taicher and Shtrikman [8] devised an inside-out NMR instrument in which a cylinder of nonconductive ferrite material was transversely magnetized, and the RF coil was wrapped along the longitudinal direction of the magnet. The resonance condition was satisfied in a thin cylindrical shell coaxial with the magnet. Kleinberg et al. [9] presented a device in which three slab magnets (two of the same size, with a third smaller magnet) were magnetized in the same direction and placed parallel with the small magnet in the center. This device provided a sensitive volume localized at a given sector with an axial extension. The antenna, which was essentially a half-coaxial cable, was placed in a semicircular cavity between the outer magnets.

In 2011, Sucre et al. [1] presented a new approach to measuring soil moisture. The sensor consisted of six cylindrical magnets (two end cylinders with a larger diameter and four centric cylinders with a smaller diameter that were magnetized perpendicular to the main axis), and a planar rectangle RF coil in the center of the magnet array. In 2013, the Sucre’s sensor was improved by Perlo et al. [10], using a five-turn rectangular RF coil with the wires placed at optimized angular positions. In this case, two cylindrical magnets with transverse polarization were utilized. The RF coil was placed in a groove on one side of the magnets. The sensitive volume in this sensor did not have an azimuthal symmetry.

Marble et al. [11] introduced a three-magnet array for single-sided NMR measurements. In this approach, three magnet blocks, which were magnetized in the same direction, were arranged to produce a homogeneous magnetic field. The magnetic field was parallel to the surface, and the design was naturally compact and safe. Even for the homogeneous magnet structure, the static field homogeneity was much less in mobile NMR devices than in conventional NMR experiments.

In this work, a mini inside-out sensor was proposed, as depicted in Figure 1. This approach combines the toroidal symmetry proposed by Jackson [7] with the advantages of the three-magnet array [11,12] concept to produce magnetic field with constant gradient in toroidal region of interest (ROI). Three arc spiral coils of the same size in series were used as the RF coil for excitation and detection. The mini NMR sensor was used to detect the moisture content of the sample that comprised soil and water. In subsequent sections, the design process of the magnet and RF coil are presented in detail, as are the experimental results.

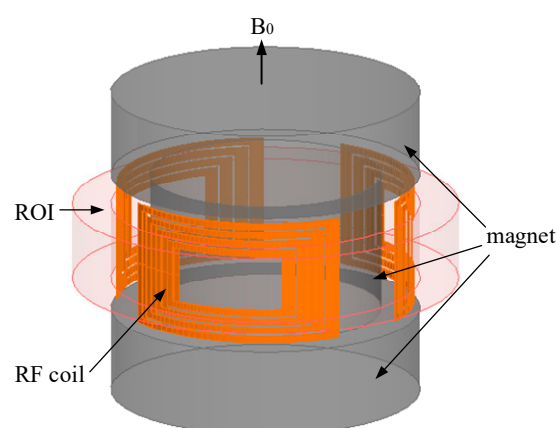


Figure 1. Mini NMR sensor model.

2. NMR Sensor Design

2.1. Magnetic Field Calculation

We derive a simple analytical calculation method for the magnetic field produced by a cylindrical magnet. This magnet is magnetized along the z -direction and positioned with its upper surface at z_2

and lower surface at z_1 , as illustrated in Figure 2a. The radius of the magnet is a , and the residual magnetization is B_r . The magnet can be represented by an equivalent surface current distributed on the cylindrical surface. The direction of current and B_r satisfy the right-hand rule. The current can be divided into infinitesimal current elements of width dz_0 , as demonstrated in Figure 2b. The magnetic field induced by each current element, as exhibited in Figure 2c, can be calculated.

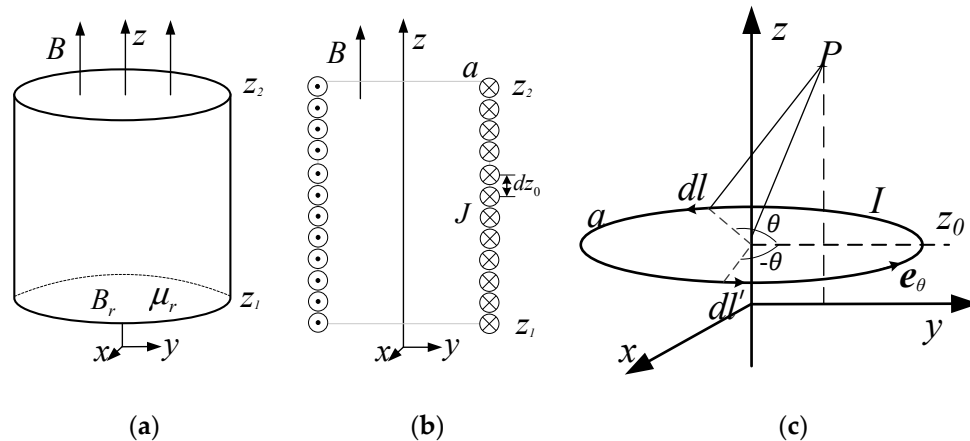


Figure 2. Calculation model of a cylindrical magnet (a). Approximation of a permanent magnet as the equivalent surface current density (b). Single-turn current for calculation (c).

For a cylindrical magnet displayed in Figure 2a, equivalent surface current density J can be written as [13]

$$J = \frac{B_r}{\mu_0} e_\theta \quad (1)$$

where B_r is the residual magnetization, μ_0 is the vacuum permeability, and e_θ is the unit vector in the circumferential direction.

The magnetic field induced by the current model presented in Figure 2c is derived by introducing the magnetic vector potential A ($B = \nabla \times A$) and using Biot–Savart’s law. The A (at field point (ρ, θ, z) in the cylindrical coordinate system) only has a circumferential component given the circumferential symmetry. It can be expressed as

$$A_\theta = \frac{\mu_0 I}{\pi k} \sqrt{\frac{a}{\rho}} \left[(1 - k^2) K(k) - E(k) \right] \quad (2)$$

where

$$k^2 = \frac{4a\rho}{\sqrt{(a+\rho)^2 + (z-z_0)^2}}, \text{ and } I \text{ is the value of the current in the coil.}$$

$$K(k) = \int_0^{\frac{\pi}{2}} \frac{d\alpha}{\sqrt{1 - k^2 \sin^2 \alpha}} \text{ is the first type of complete elliptic integral.}$$

$$E(k) = \int_0^{\frac{\pi}{2}} \sqrt{1 - k^2 \sin^2 \alpha} d\alpha \text{ is the second type of complete elliptic integral.}$$

On the basis of $B = \nabla \times A$, we can obtain magnetic flux density B induced by a single-turn coil driven by a constant current I .

$$B_\rho = \frac{\mu_0 I}{2\pi} \frac{z}{\rho \sqrt{(a+\rho)^2 + (z-z_0)^2}} \left[-K(k) + \frac{a^2 + \rho^2 + (z-z_0)^2}{(a-\rho)^2 + (z-z_0)^2} E(k) \right] \quad (3)$$

$$B_z = \frac{\mu_0 I}{2\pi} \frac{1}{\sqrt{(a+\rho)^2 + (z-z_0)^2}} \left[K(k) + \frac{a^2 - \rho^2 - (z-z_0)^2}{(a-\rho)^2 + (z-z_0)^2} E(k) \right] \quad (4)$$

In Equations (3) and (4), I is replaced with $B_r/\mu_0 \cdot dz_0$, and the variable z_0 is considered integral in the interval $[z_1, z_2]$. The magnetic flux density \mathbf{B} induced by the cylindrical magnet can be written as

$$B_\rho = \frac{B_r}{2\pi} \int_{z_1}^{z_2} \frac{z}{\rho \sqrt{(a+\rho)^2 + (z-z_0)^2}} \left[-K(k) + \frac{a^2 + \rho^2 + (z-z_0)^2}{(a-\rho)^2 + (z-z_0)^2} E(k) \right] dz_0 \quad (5)$$

$$B_z = \frac{B_r}{2\pi} \int_{z_1}^{z_2} \frac{1}{\sqrt{(a+\rho)^2 + (z-z_0)^2}} \left[K(k) + \frac{a^2 - \rho^2 - (z-z_0)^2}{(a-\rho)^2 + (z-z_0)^2} E(k) \right] dz_0 \quad (6)$$

2.2. Magnet Structure Optimization and Field Measurement

The construction of the magnet array of the mini NMR sensor is depicted in Figure 1. The sensor consists of three cylindrical magnets that are magnetized in the z -axis, and the diameter of the magnet is smaller in the center than at the ends to leave a certain space for the RF coil.

According to electromagnetic field theory, in the region near the magnet surface, two separated magnets produce an increasing field centered above and between them, whereas another magnet placed between them produces a decreasing field centered above [11,14]. The first or second derivatives of the static magnetic field in the ROI along the radial direction can be adjusted to 0 by properly adjusting the parameters of the three magnets (Figure 1). Homogeneous magnetic fields or magnetic fields with constant gradient can be induced using the three magnets. Thus, the parameters that must be optimized include the diameter and height of each magnet. Considering engineering applications, we limited the diameter and height of the sensor to at most 40 and 100 mm, respectively.

YXG32 $\text{Sm}_2(\text{CoFeCuZr})_{17}$ cylindrical magnets (Ninggang Permanent Magnetic Materials Co., Ltd., Ningbo, Zhejiang, China) were applied, because this type of permanent magnet has a low temperature coefficient ($-0.035\%/^\circ\text{C}$) and high remanence (B_r 1.10–1.13 Tesla). Based on optimization, the central cylinder was 26 mm in diameter and 24 mm in length, whereas the two end cylinders were 30 mm in diameter and 10 mm in length. The titanium alloy housing used for fixing magnets has a diameter of 40 mm.

The magnetic field was measured using a BELL 8030 Hall probe and a computer-controlled three-axis position system. Figure 3 illustrated a contour plot of the magnetic field magnitude around the magnet array. The position $\rho = 20$ (where $\rho^2 = x^2 + y^2$) corresponds to the outside surface of the sensor. Slight asymmetry was noted given the unequal magnetizations of the magnets and measurement errors. However, the field in the ROI was reasonably symmetric. Figure 4 plots the magnitude of the magnetic field as a function of depth over the center of magnets. The approximately constant gradient at the region that occurs within 10 mm from the magnet surface corresponded to the ROI. The field gradient remains within the 2.28 T/m range over the region more than 10 mm deep.

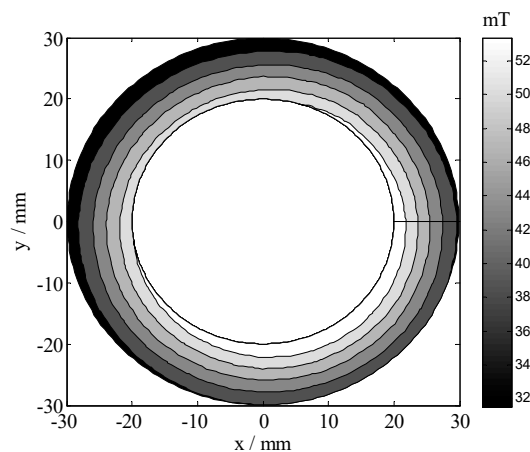


Figure 3. Magnetic field measured using a gauss meter in the ROI.

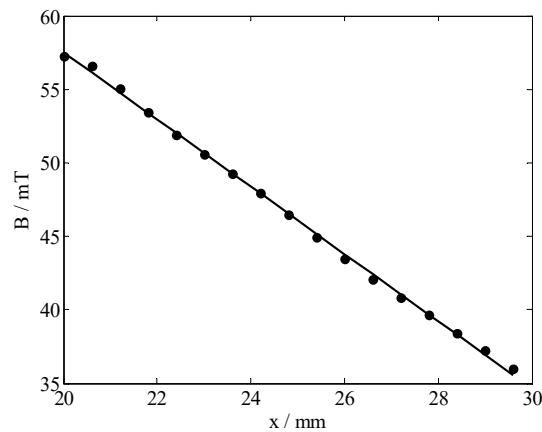


Figure 4. Magnitude of the magnetic field as a function of depth over the center of magnets.

2.3. RF Coil Design

To excite hydrogen and receive as many signals as possible in the ROI, three arc spiral coils of the same size connected in series (Figure 5) were used as the RF coil. Based on reference [15], when the experimental environment and the B_0 remained the same, the SNR was proportional to the B_1 generated by the RF coil and inversely proportional to the current through the RF coil and the square root of the AC resistance of the coil, as in Equation (7).

$$\text{SNR} \propto \frac{B_1/i}{\sqrt{R}} \cdot V_{\text{sample}} \quad (7)$$

where V_{sample} is the effective sample volume; R is the combined noise resistance of coil, sample, and spectrometer electronics; and B_1/i is the coil sensitivity defined by the law of reciprocity as the magnetic flux density B_1 caused by an RF current i that passes through the coil. We defined the right side of Equation (7) as the relative SNR for evaluating the RF coil.

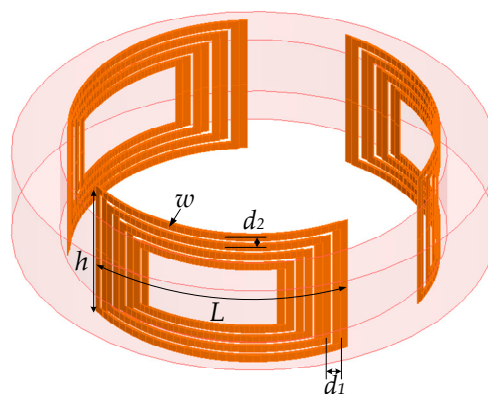


Figure 5. RF coil model. The arc length of each arc spiral coil with N turns is L , the width of wire is w , the height of wire is h , and the spacing of the adjacent wires along the circumference and z -direction is d_1 and d_2 , correspondingly.

To facilitate the installation of the RF coil, we printed it on a flexible printed circuit board (fPCB). The effective value of the AC current was set to 1 A at 2 MHz, and the values of B_1 produced by the RF coil and R were calculated using the simulation software Maxwell 3D (ANSYS, Inc., Canonsburg, PA, USA). By varying the parameters of the RF coil, the optimal RF coil was limited by the size of the magnet body and shell, the wiring area of the arc spiral coil achieved relatively homogeneous excitation and signal reception across the sensitive volume. The parameters of RF coils that must be optimized include the turns of the coil, the distance between adjacent wires, and the width of wires. We simulated

dozens of coils, and Figure 6 demonstrates the results of three of these models. The optimal coil is Model 1. Finally, this mini sensor is 40 mm in diameter and 100 mm in length and is portable for soil moisture measurements on-field.

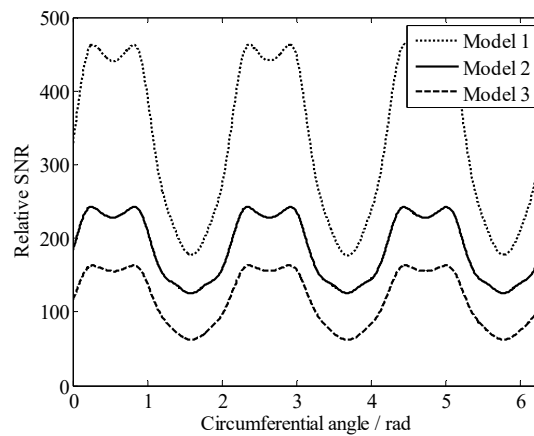


Figure 6. Relative SNRs of the RF coils with different structure parameters, where, parameters of Model 1 are $N = 4$, $L = 28$ mm, $h = 15.2$ mm, $w = 0.8$ mm, $d_1 = 2$ mm, and $d_2 = 1.2$ mm; parameters of Model 2 are $N = 6$, $L = 32.3$ mm, $h = 15.2$ mm, $w = 0.6$ mm, $d_1 = 1.5$ mm, and $d_2 = 0.9$ mm; and parameters of Model 3 are $N = 6$, $L = 34.3$ mm, $h = 15.2$ mm, $w = 0.6$ mm, $d_1 = 1.5$ mm, and $d_2 = 0.9$ mm.

3. Results and Discussion

In this work, we selected sandy soil and silica sand (shown in Figure 7) with water to prepare an experimental sample, and then we measured them through Carr–Purcell–Meiboom–Gill (CPMG) measurements and weighing analysis to determine the moisture content of this sample. The moisture content η could be determined through the weighing method.

$$\eta = \frac{m_1 - m_2}{m_1} \times 100\% \quad (8)$$

where m_1 is the weight of the sample with water, and m_2 is the weight of the sample without water, the weight is measured by an electronic balance (precision is 0.001 g).

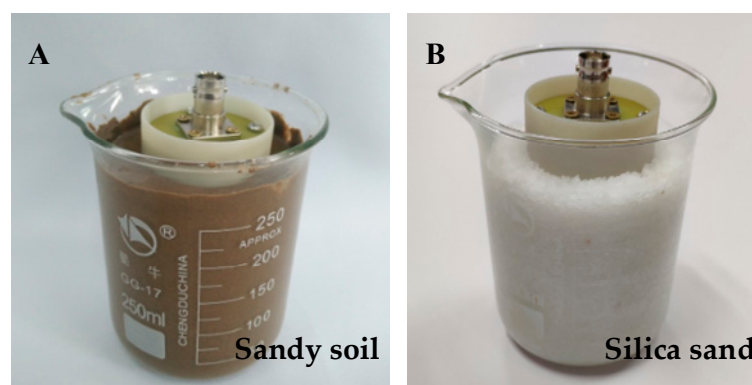


Figure 7. Sandy soil and silica sand.

Sample A is a mixture of sandy soil (219.613 g in weight, particle diameter is smaller than 0.25 mm) and water (38.538 g in weight), the initial moisture content is 17.55%. Sample B is a mixture of silica sand (216.367 g in weight, particle diameter is between 0.85 mm and 2 mm) and water (62.004 g in weight), the initial moisture content is 22.27%. To measure the samples with different moisture contents, we dried it continuously in a humidity chamber. The temperature in the humidity chamber was 40 °C for drying the samples.

The mini sensor was set at a certain depth to measure the water content of the soil sample. Experiments were conducted through a Magritek Kea2 Spectroscopy (Wellington, New Zealand), which consists of an internal preamplifier and lumped element duplexer. The measurement system is depicted in Figure 8. A total of 2100 echoes from the sample were obtained in 2048 scans through the CPMG experiment; the 90° and 180° pulse widths were $12 \mu\text{s}$, the NMR frequency was 2.424 MHz, and the echo time was $120 \mu\text{s}$. Figure 9 displays a CPMG decay measured using 2048 signal sums. The complete decaying NMR signal is analyzed through inverse Laplace transformation and averaged on a T_2 space.

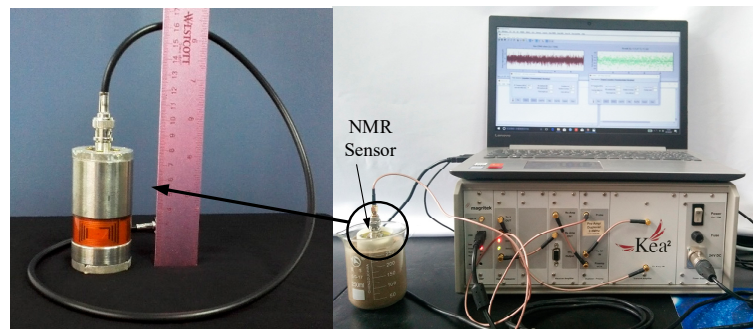


Figure 8. Measurement system.

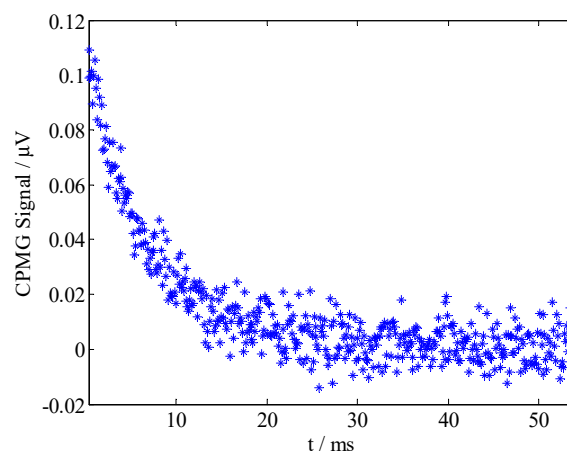


Figure 9. T_2 decay measured using a CPMG sequence for sample A (moisture content is 8.53%).

The CPMG decays are analyzed in terms of multiple exponential fitting [16]

$$y(t) = \sum_{j=1}^m f(T_{2j})e^{-t/T_{2j}} + \zeta(t), \quad (9)$$

where $y(t)$ is amplitude of CPMG signal at t , $f(T_{2j})$ is the amplitude of component with transverse relaxation time T_{2j} , $\zeta(t)$ is stochastic noise, m is the number of relaxation components, and T_2 spectrum curve is the relationship between T_2 with $f(T_2)$. The integral area (A_{peak}) of peak in T_2 spectrum curve can be expressed as

$$A_{peak} = \int_{T_{2min}}^{T_{2max}} f(T_2)dT_2, \quad (10)$$

Thus, by substituting the measured data into Equation (9), we can obtain the T_2 spectrum $f(T_2)$. The T_2 spectrum of sample A (moisture content is 8.53%) is presented in Figure 10. To verify performance of the sensor, we measured sample A (moisture content is 8.53%) five times, A_{peak} are 0.8904, 0.8759, 0.8636, 0.8675, and 0.8384, respectively; averaging at 0.8672, the maximum deviation ratio ($|A_{peak} - \bar{A}_{peak}| / \bar{A}_{peak} \times 100\%$) is 3.32%.

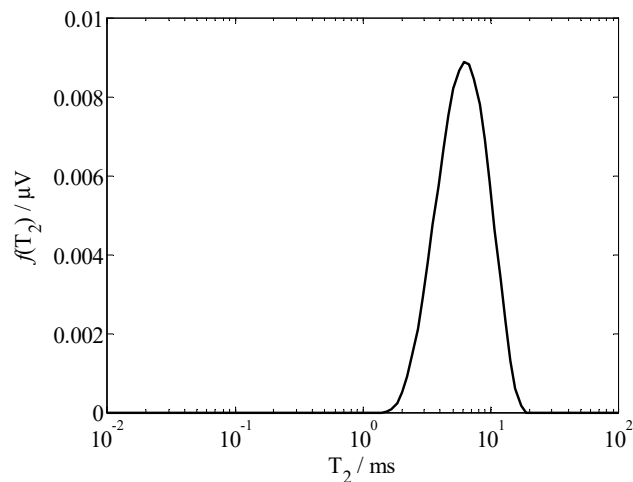


Figure 10. T_2 spectrum curves of sample A (moisture content is 8.53%).

Considering graph visualization, Figures 11 and 12 only illustrates five results of different moisture contents, although we measured the samples every hour throughout the day. According to Figures 11 and 12, we know that the position of the T_2 spectrum peak shifted to the left gradually with the decrease of moisture. To further study the relationship between moisture content and T_2 spectrum, we calculated the integral area of each spectrum peak (A_{peak}), then graph the relationship between A_{peak} with T_2 , illustrated in Figures 13 and 14. These curves could indicate the integral area of the T_2 spectrum, which is positively correlated with moisture content.

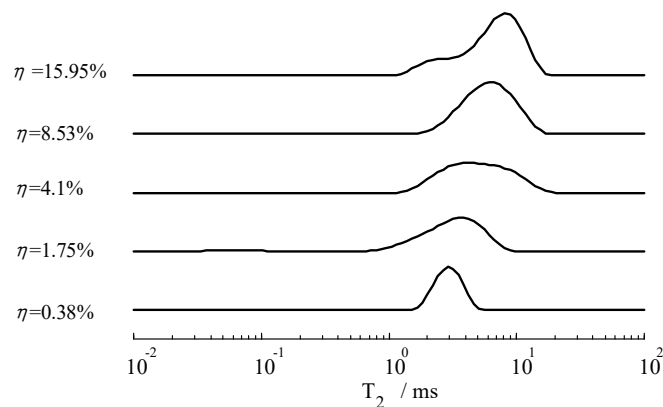


Figure 11. T_2 spectrum curves of the sandy soil with different moisture content.

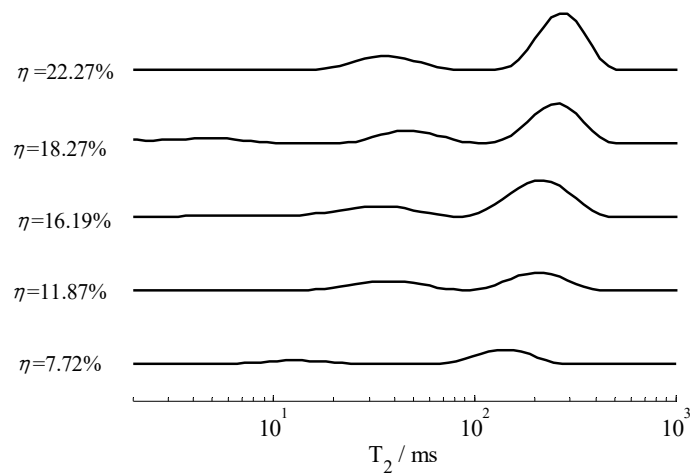


Figure 12. T_2 spectrum curves of the silica sand with different moisture content.

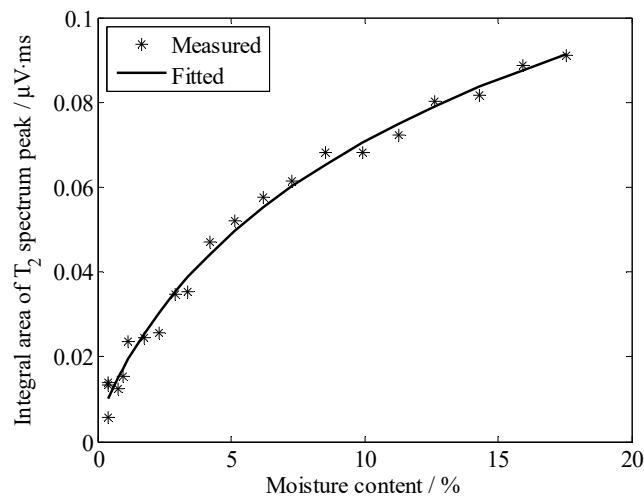


Figure 13. Correspondence between the integral area of the T_2 spectrum with the moisture content of the sandy soil.

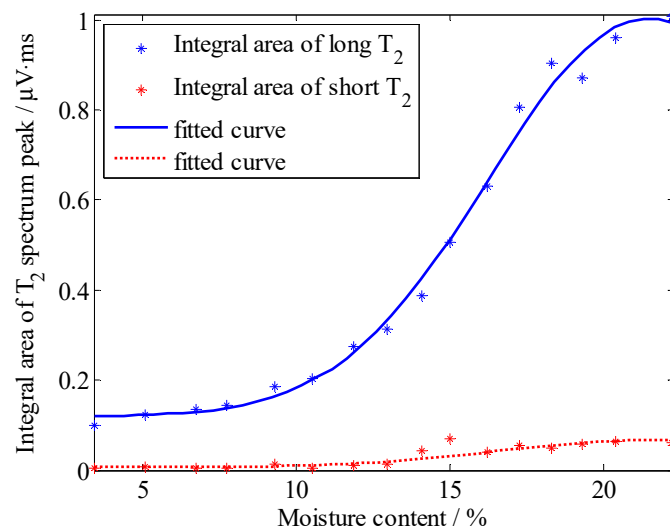


Figure 14. Correspondence between the integral area of the T_2 spectrum with the moisture content of the silica sand.

According to Figures 11 and 12, the T_2 spectrum curves of the sandy soil only have one peak, whereas the T_2 spectrum curves of the silica sand have two peaks (a long T_2 peak and a short T_2 peak). The reason for this phenomenon is that particle diameter of sandy soil is almost the same size and the pore size is basically the same, while particle diameter of silica sand is 0.85~2 mm and sample include large pores and small pores. T_2 of the water in small pores is shorter than that in large pores, because the movement of water molecules are limited by inner wall of the pores. In the same volume, there is more water in the large pore sample is than in the small pore sample, so A_{peak} of silica sand is larger than A_{peak} of sandy soil. In Figures 13 and 14, the results indicate that A_{peak} of the large pore sample (silica sand) is more sensitive to represent the changes in moisture than that of the small pore sample (sandy soil) when moisture content is high, and A_{peak} of the small pore sample (sandy soil) is more sensitive to represent the changes in moisture than that of the large pore sample (silica sand) when moisture content is low.

4. Conclusions

In this work, we presented a mini NMR sensor that combines three cylindrical magnets to measure moisture content effectively in sandy soil and silica sand. The sensor has a constant gradient

of 2.28 T/m. A novel RF coil composed of three arc spiral coils of the same size connected in series was designed for inside-out NMR applications. The coil demonstrated a high SNR, mostly due to an enhancement in the sensitivity region. The complete decaying NMR signal was analyzed through inverse Laplace transformation on the T_2 space, which could estimate the moisture content of the samples. This mini sensor is portable, and the sensitive region is relatively larger than its actual size. In conclusion, this mini NMR sensor has been demonstrated to be a fast and a noninvasive technique for investigating the moisture content of soils. Moreover, this mini sensor may allow easy on-field soil moisture measurements in the future. Further research should focus on applying this sensor to pore media measurement, thereby improving stability and detection depth by further optimizing the sensor structure.

Author Contributions: Conceptualization, J.W. and P.G.; methodology, J.W. and Y.H.; software, Y.H.; validation, Z.X.; formal analysis, J.W. and S.S.; investigation, J.W. and P.G.; resources, Z.X. and P.G.; data curation, S.S.; writing—original draft preparation, J.W.; writing—review and editing, J.W. and P.G.; visualization, X.H.; supervision, Z.X.; project administration, Z.X.; funding acquisition, Z.X. and P.G.

Funding: This research was funded by the National Natural Science Foundation of China (No. 51677008 and 51707028), Fundamental Research Funds for the Central Universities (No. 2018CDJDDQ0017), and Science and Technology Funds of Chongqing Municipal Education Commission (KJ1600333).

Conflicts of Interest: The authors declare no conflict of interest.

References

1. Sucre, O.; Pohlmeier, A.; Minière, A.; Blümich, B. Low-field NMR logging sensor for measuring hydraulic parameters of model soils. *J. Hydrol.* **2011**, *406*, 30–38. [[CrossRef](#)]
2. Alvarado, R.J.; Damgaard, A.; Hansen, P.; Raven, M.; Heidler, R.; Hoshun, R.; Kovats, J.; Morriss, C.; Rose, D.; Wendt, W. Nuclear magnetic resonance logging while drilling. *Oilfield Rev.* **2003**, *15*, 40–51.
3. Blümich, B.; Perlo, J.; Casanova, F. Mobile single-sided NMR. *Prog. Nucl. Magn. Reson. Spectrosc.* **2008**, *52*, 197–269. [[CrossRef](#)]
4. Behroozmand, A.A.; Keating, K.; Auken, E. A Review of the principles and applications of the NMR technique for near-surface characterization. *Surv. Geophys.* **2015**, *36*, 27–85. [[CrossRef](#)]
5. Blank, A.; Alexandrowicz, G.; Muchnik, L.; Tidhar, G.; Schneiderman, J.; Virmani, R.; Golan, E. Miniature self-contained intravascular magnetic resonance (IVMI) probe for clinical applications. *Magn. Reson. Med.* **2005**, *54*, 105–112. [[CrossRef](#)] [[PubMed](#)]
6. Burnett, L.J.; Jackson, J.A. Remote (inside-out) NMR. I. Remote production of a region of homogeneous magnetic field. *J. Magn. Reson.* **1980**, *41*, 406–410.
7. Jackson, J.A.; Lowell, J.B.; Harmon, J.F. Remote (inside-out) NMR. III. Detection of nuclear magnetic resonance in a remotely produced region of homogeneous magnetic field. *J. Magn. Reson.* **1980**, *41*, 411–421. [[CrossRef](#)]
8. Taicher, Z.; Shtrikman, S. Nuclear Magnetic Resonance Sensing Apparatus and Techniques. U.S. Patent No. 4,717,877, 5 January 1988.
9. Kleinberg, R.L.; Sezginer, A.; Griffin, D.D.; Fukuhara, M. Novel NMR Apparatus for investigating an external sample. *J. Magn. Reson.* **1992**, *97*, 466–485. [[CrossRef](#)]
10. Perlo, J.; Danieli, E.; Perlo, J.; Blümich, B.; Casanova, F. Optimized slim-line logging NMR tool to measure soil moisture in situ. *J. Magn. Reson.* **2013**, *233*, 74–79. [[CrossRef](#)] [[PubMed](#)]
11. Marble, A.E.; Mastikhin, I.V.; Colpitts, B.G.; Balcom, B.J. A compact permanent magnet array with a remote homogeneous field. *J. Magn. Reson.* **2007**, *186*, 100–104. [[CrossRef](#)] [[PubMed](#)]
12. Guo, P.; He, W.; Juan, C.G.; Bruce, J.B. A New inside-out nuclear magnetic resonance sensor—Three-cylinder array. *Trans. China Electrotech. Soc.* **2016**, *31*, 96–101.
13. Jackson, J.D. *Classical Electrodynamics*, 3rd ed.; John Wiley & Sons, Inc.: Hoboken, NJ, USA, 1999; pp. 184–194.
14. García-Naranjo, J.C.; Mastikhin, I.V.; Colpitts, B.G.; Balcom, B.J. A unilateral magnet with an extended constant magnetic field gradient. *J. Magn. Reson.* **2010**, *207*, 337–344. [[CrossRef](#)] [[PubMed](#)]

15. Watzlaw, J.; Glöggler, S.; Blümich, B.; Mokwa, W.; Schnakenberg, U. Stacked planar micro coils for single-sided NMR applications. *J. Magn. Reson.* **2013**, *230*, 176–185. [[CrossRef](#)] [[PubMed](#)]
16. Chelcea, R.I.; Fehete, R.; Culea, E.; Demco, D.E.; Blümich, B. Distributions of transverse relaxation times for soft-solids measured in strongly inhomogeneous magnetic fields. *J. Magn. Reson.* **2009**, *196*, 178–190. [[CrossRef](#)] [[PubMed](#)]



© 2019 by the authors. Licensee MDPI, Basel, Switzerland. This article is an open access article distributed under the terms and conditions of the Creative Commons Attribution (CC BY) license (<http://creativecommons.org/licenses/by/4.0/>).